Acta Materialia 95 (2015) 386–398

Contents lists available at ScienceDirect

Acta Materialia

journal homepage: www.elsevier.com/locate/actamat

Alloying effects on microstructure formation of dual phase steels

L. Schemmann [a,1], S. Zaefferer [a,*], D. Raabe [a], F. Friedel [b], D. Mattissen [b]

[a] Max-Planck-Institut für Eisenforschung, Düsseldorf, Germany
[b] ThyssenKrupp Steel Europe AG, Duisburg, Germany

ARTICLE INFO

Article history:
Received 21 November 2014
Revised 7 March 2015
Accepted 4 May 2015

Keywords:
DP steel
Geometrically necessary dislocations
Gamma–alpha phase transformation
Mn distribution
DICTRA

ABSTRACT

In dual-phase (DP) steels, inherited microstructures and elemental distributions affect the kinetics and morphology of phase transformation phenomena and the mechanical properties of the final material. In order to study the inheritance process, we selected two model materials with the same average DP steel composition but with different initial microstructures, created by coiling at different temperatures after hot rolling. These samples were submitted to a DP-steel heat treatment consisting of a short isothermal annealing in the pure austenite region and a quenching process. The evolution of microstructure, chemical composition and mechanical properties (hardness) during this treatment was investigated.

The initial samples had a bainitic–martensitic (B + M) microstructure for the material coiled at lower temperature and a ferritic–pearlitic (P + F) microstructure for that coiled at higher temperature. The P + F microstructure had a much more inhomogeneous distribution of substitutional elements (in particular of Mn) and of carbon. After complete heat treatment, both materials showed a typical DP microstructure (martensite islands embedded in ferrite) but the P + F material showed lower hardness compared to the B + M material. It was found that the inhomogeneous elemental distribution prevailed in the P + F material.

The inheritance process was studied by combining measurements of the elemental distribution by Wavelength-Dispersive X-ray spectroscopy (WDX), simulations of the evolution of the elemental composition via the DICTRA (diffusion-controlled reactions) computer programme, dilatometry to observe the kinetics of phase transformation, and observation and quantification of the microstructures by Electron Backscatter Diffraction (EBSD) measurements. For the P + F material it was found that the α–γ transformation during annealing is slowed down in regions of lower Mn content and is therefore not completed. During the subsequent cooling the incompletely autenitized material does not require ferrite nucleation and the γ–α transformation starts at relative high temperatures. For B + M, in contrast, nucleation of ferrite is needed and the transformation starts at lower temperatures. As a result the B + M material develops a higher martensite content as well as a higher density of geometrically necessary dislocations (GNDs). It is speculated that for the B + M material the γ–α transformation occurs through a bainitic (i.e. partly displacive) process while the transformation at higher temperatures in the P + F material proceeds exclusively in a diffusive way.

1. Introduction

Dual-phase steels consist of martensite islands embedded in a ferrite matrix. Typically, the martensite volume fraction is around 15–25% [1–5]. They are synthesized from a rather lean elemental composition (e.g. approx. 0.2 wt.% C, 1.5 wt.% Mn and 0.25% Si [6]) via an intercritical heat treatment in the austenite (γ)–ferrite (α) two-phase region followed by quenching the material. The good mechanical properties [1,7,8] combined with low costs make DP steels attractive as structural design materials. A number of works have addressed the optimization of the thermomechanical heat treatment [3,9–11] and the resulting microstructures [7,12–14] and properties [12,15–18] of these steels. For instance, Calcagnotto et al. used different heat treatments to lower the grain size of ferrite, since this improves the toughness of the DP-steel and the capability to absorb impact energy [13]. Also the initial microstructure of the steel before intercritical annealing controls, in different ways, the properties of a dual phase steel [7,19–25].

Different initial microstructures may be related to different elemental distribution in the material and may influence the properties of the final material. The heterogeneous spatial distribution of substitutional elements, in particular, is of great importance for the properties of DP-steels. Manganese crystal-segregations from

* Corresponding author.
[1] Current affiliation: Salzgitter-Mannesmann Forschung, Duisburg, Germany.

http://dx.doi.org/10.1016/j.actamat.2015.05.005
1359-6454/

solidification, for example, are stretched out during rolling, leading to microstructures where the carbon-rich phases like pearlite, bainite or martensite are confined to those band-like areas which have a higher Mn-content. [23–26]. An inhomogeneous manganese distribution is not only found on the micrometer scale, where it is caused by solidification segregations, but also on the sub-micro- to nanometer scale. Here it is related to globular cementite or lamellar cementite in pearlite [22,27–29]. Cai et al. [22] described the influence of different starting microstructures on the formation of a dual phase steel. To obtain the starting microstructures, they applied several heat treatments to different samples of the same type of steel. One of the applied heat treatments led to a pearlite microstructure, in which the cementite lamellae were enriched with Mn. They report that the cementite in pearlite must have formed under conditions of low carbon supersaturation, since these conditions are the only ones at which substantial partitioning of Mn can occur. During the intercritical annealing, which they applied to the pearlite-containing microstructure, these Mn-enrichments did not dissolve completely and after complete heat treatment a duplex microstructure consisting of ferrite and austenite/martensite was present. Calcagnotto et al. [30] described the influence of globular cementite on the formation of a dual phase steel. They showed, that Mn-enrichments, caused by globular cementite, survive an intercritical annealing and enrichments can be found afterwards in austenite where they raise the hardenability. Apart from these two papers, little information related to the inheritance of elemental distribution has been found in the literature.

The scope of this study is to understand the influence of an inhomogeneous local distribution of Mn, related to individual carbide precipitates and to cementite in pearlite, on the reaustenization process of a dual-phase steel and on its mechanical properties after final heat treatment. Therefore, two different initial microstructures were created from a steel with typical DP-steel composition by using different coiling regimes after hot rolling. Afterwards, the same heat treatment, including an isothermal annealing above the AC3 temperature, was applied to both materials. The evolution of microstructure and elemental distribution was investigated using light optical microscopy (LOM), Scanning Electron Microscopy (SEM) with Electron Backscatter Diffraction (EBSD), Energy Dispersive X-ray spectroscopy (EDX), Wavelength Dispersive X-ray spectroscopy (WDX), dilatometry and hardness measurements. This was done at different stages during the heat treatment. The evolution of local Mn-enrichments during the heat treatment and the influence on the local phase transformation was furthermore investigated by thermodynamical simulations. For equilibrium calculations, ThermoCalc (TC) was used and simulations diffusional phase transformations were performed with DICTRA (TC) [31,32].

2. Experimental methods

2.1. Material production

A commercial hot rolled steel with a typical DP-steel composition of 0.14 wt.% C, 1.9 wt.% Mn and 0.4 wt.% Cr, 0.25 wt.% Si was used as initial material in the form of 3.7 mm thick plates. Different initial microstructures were created by a variation of the coiling temperature after hot rolling during large-scale industrial production of the material. Note that the exact coiling temperatures cannot be given but they are below the AC1 temperature and differ by about 100 K. For the microstructural investigations and heat treatments, cylinders were cut from the material with a diameter of 4 mm and a length of 9 mm. The rolling direction was parallel to the cylinder axis. Since the total thickness of the sheet was slightly lower than 4 mm the cylinder had flat surfaces perpendicular to the normal direction.

All heat treatments were performed in a dilatometer (DIL 805A/D produced by TA Instruments) equipped with an induction heater. During heat treatments, an argon atmosphere was established in the dilatometer to prevent the material from oxidization. The thermal treatment is sketched in Fig. 1. A maximum temperature of 840 °C was applied for roughly 90 s. In total, the heat treatment took less than 10 min. In order to follow the evolution of the properties of the material, samples from 3 different stages were observed, as shown in Fig. 1: the initial material (point 1), material quenched after the isothermal holding (point 2) and final material after complete heat treatment (point 3).

2.2. Microstructural investigations

For microstructural investigations specimens were cut along the normal direction–rolling direction plane. Specimens were ground, polished until 3 μm and etched with 1 pct. Nital. Both, LOM and SEM were used for microstructural investigations.

The average austenite content was measured using X-ray diffraction (XRD). A Seifert Type ID 3003XRD system with a Meteor0D detector produced by General Electric was employed. The spectra were evaluated using the MAUD software package in version 2.33 [33]. The specimens were ground, polished until 3 μm and polished with Oxide Polishing Suspension (OPS).

EBSD was used to observe the distribution of ferrite, martensite and austenite. Specimens were prepared in the same way as those of LOM and XRD-analyses. A Zeiss-Crossbeam XB 1540-SEM equipped with an EDX silicon drift detector (Apollo XL) and an EBSD system with a Hikari camera provided by EDAX were used. The measurements were performed at an accelerating voltage of 15 kV and mostly with 100 nm step size. EBSD data were analysed with TSL OIM software version 6.2. Measurement points with a confidence index lower than 0.1 were excluded from the measurement [34], whereby the confidence index is a criterion of the reliability of the indexing of a given EBSD pattern.

The distinction between ferrite and austenite is straightforward, as they differ in crystal structure. In contrast, the separation between martensite and ferrite by EBSD is more challenging, since the crystal structure of martensite and ferrite cannot be distinguished by conventional EBSD. In this paper, both were separated using the grain average image quality (IQ), as is described in detail by Pinard et al. [35]. The IQ is a measure for the quality of a diffraction pattern [36]. Martensite has a higher defect density than ferrite and shows, therefore, a clearly lower IQ value than ferrite. To exclude the effect of grain boundaries, which show a low IQ as well, the "grain average (GA) IQ"-value was used. Since, in the present material, martensite and ferrite do not yield very different IQ values, the GA-IQ-value distribution is not sharply bimodal. Selecting the correct IQ threshold value for the differentiation between ferrite and martensite, therefore, is not unique. Thus, upper and lower values for the martensite content were determined and the average of both was set as the martensite content. As error for this procedure we selected half of the difference between upper and lower values. A quantitative and statistically representative measurement of the average martensite content of the material was performed by using a large area EBSD scan as described by Davut et al. [37].

The performed heat treatment led to the formation of geometrically necessary dislocations (GND). Their density was determined using kernel average misorientation (KAM) calculations. In OIM data analysis (version 6.2) the KAM value is calculated from orientation maps as the average over all misorientation angles determined between a centre pixel and all its neighbours, thereby excluding pairs with larger misorientations than a defined

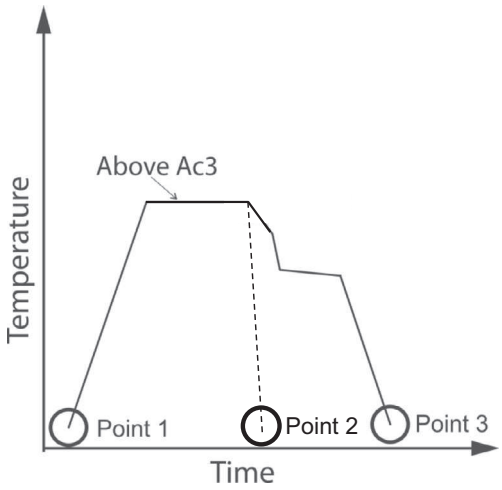

Fig. 1. Sketch of the applied heat treatments.

threshold angle. In this paper, the threshold was set to 4°. In the software it is also possible to define the size of the kernel. During this study only the direct neighbours of a measurement point were taken into account. KAM values obtained from different measurements are only comparable, if the measurement step size is the same.

There exist several ways to calculate the GND density from KAM values. In a study presented by Calcagnotto et al. [38] a method was used which is based on the work of Kubin and Mortensen [39]. Under the assumption that a series of twist subgrain boundaries in a cylinder contains two perpendicular arrays of screw dislocations, the GND density can be calculated as follows:

$$\rho_{GND} = \frac{2\theta}{ub}, \tag{1}$$

where θ is the misorientation angle, u is the unit length and b is the magnitude of the Burgers vector. Here, the KAM value is used as an approximation for the misorientation angle. For an EBSD measurement, $u = a \cdot n$, with a being the step size, a, and n the level of "neighborhoodness" (first, second, or nth neighbour) in the kernel. For the bcc-material the length of the Burgers vector is $b = \frac{d}{2}\sqrt{3}$, with d being the lattice constant of the unit cell. For the present material the bcc lattice cell constant was determined by XRD to be 0.2867 nm.

2.3. Chemical analysis

The distribution of the substitutional elements as well as carbon was measured with a JEOL tungsten Microprobe (JXA-8100). This instrument is equipped with 4 WDS-detectors. Here the sample preparation was the same as that of EBSD. The spatial resolution WDX and EDX depends strongly on the accelerating voltage of the electron beam [42] and on the energy of the analysed characteristic X-ray line. To take this into account, the following equation was used to find the optimum step size [42].

$$Z_m = 0.033 \cdot \frac{(E_0^2 - E_c^2)}{\rho}.$$

Z_m is the lateral resolution in μm, E_c is the energy of the characteristic X-ray line, E_0 the energy of the electron beam and ρ is the density of the material. For iron ($\rho_{Fe} = 7.874\ \frac{g}{cm^2}$), an accelerating voltage of 12 kV and the Kα line of Mn ($E_{c\,Mn} = 6,539$ eV) [42] this delivers a spatial resolution of $Z_{m\,Mn} = 424$ nm To avoid too much overlap between two pixels in the mapping, most of the measurements were performed with a step size of 300 nm. To perform quantification with standards at least two samples with a known concentration level are needed. This allows correlating the measured count rate with concentration. For manganese pure iron is used as a first standard. As a second standard the sample itself with its known average composition was employed and it was assumed that a measurement on a large area will return this average composition for manganese as well as that of carbon. As a second standard for carbon the average count rate of pearlite was chosen. Assuming a eutectoid pearlite, its carbon concentration is well known to be 0.8 wt.%. Carbon contamination during WDX measurements is a serious challenge, since it reduces the reliability of carbon measurements. As proposed by Eichen et al. [43] a trap cooled by liquid nitrogen below the pole piece was used during this research. In order to lower the contamination rate even more, the specimens were inserted into the microprobe one day before the measurement.

For analysing the exact composition of the carbides present in the steel, extraction replica were prepared. The technique applied in this study is similar to the one described in [44]. Specimens were polished in the same way as they were for EBSD. Subsequently they were etched with a 2 pct. Nital solution for 30 s, coated with carbon by evaporation and then covered with a deposition of ethyl acetate. After drying, the varnish was cut into small pieces using a scalpel and dipped into distilled water and nitric acid until the extraction replica lost contact to the surface. Finally, the extraction replicas were taken out of water, deposited on copper TEM-grids and dried.

For analysis of the extraction replica, the same microscope was used as that of EBSD measurements. EBSD and EDX were combined to reveal the type of carbide and its composition. For quantitative EDX analysis the peak to background method was applied [42]. EBSD analysis was carried out on a 70° tilted sample with an accelerating voltage of 30 kV. This high accelerating voltage delivered the best EBSD patterns for carbides. Afterwards the specimens were tilted back to 0° and the composition of the carbides was analysed with EDX in spot mode.

In order to determine the amount of carbides in the microstructure after complete heat treatment, EDX mappings were performed in SEM–STEM mode. The measurement of the Fe, Mn, Cr and Ti signal allowed distinction of Fe–Cr–Mn-carbides, Ti-carbo nitrides and contamination caused by the preparation process. The fraction of the carbides was measured based on large EDX maps obtained with a remote-control script of OIM Data collection (Version 6.2).

2.4. Other experimental observations

For hardness measurements, the specimens were prepared in the same way as those of SEM analysis. All hardness values were measured with a microindentation hardness testing system (LM 100 AT) supplied by the company Leco, applying a load of around 9.81 N (HV1). For every shown hardness value, 6 different measurements were performed and the average value was taken. The error is the standard deviation of the measurements.

TEM specimens were produced by focused ion beam (FIB) target preparation using an FEI Helios NanoLab 600 dual beam instrument consisting of an FIB milling system and an FEG electron gun. Diffraction in TEM was performed in a JEOL JEM 2200FS using the ASTAR package supplied by NanoMEGAS [40,41].

2.5. Simulation methods

All phase diagrams shown in this paper and all thermodynamic equilibrium calculations were created by using the commercial package of Thermo-Calc (Version 3.1) [45]. The TCFE 7 database was used. Moving phase boundaries and diffusional problems were

calculated with DICTRA. In order to perform the calculations, the database MOBFE2 was used.

3. Results

3.1. Optical microscopy and hardness measurements

Fig. 2(a) and (b) presents SEM-images of the two different starting microstructures after slight etching. In the case of P + F (Fig. 2(a)), the pearlite islands and single carbides located in the ferrite matrix are clearly visible. Fig. 2(b) shows the B + M microstructure before heat treatment. Here, a mixture of martensite, bainite and ferrite is present. The P + F microstructure forms, when coiling is performed at high temperatures. The B + M microstructure is formed at about 100 K lower temperatures. After complete heat treatment, both microstructures show a martensite–ferrite dual phase structure (cf. Fig. 2(c) and (d)).

The hardness measurements (cf. Fig. 3) show that the B + M microstructure before heat treatment is about 20% harder than the P + F microstructure. At the end of the plateau (Point 2), both microstructures have nearly the same hardness. The complete heat treatment leads again to a higher hardness of the B + M microstructure (about 10% higher).

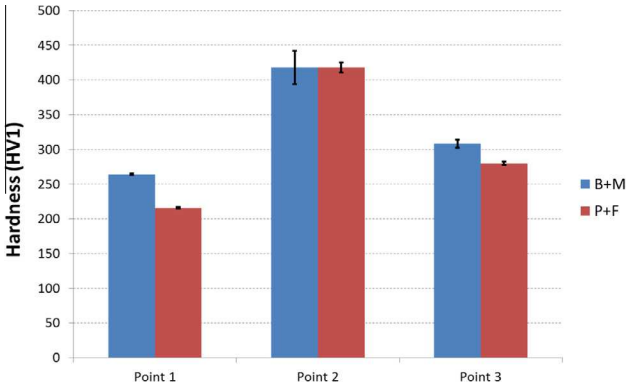

Fig. 3. Hardness of the two different microstructures at different points (see Fig. 1) of the heat treatments.

3.2. Analysis of the distribution of the substitutional elements

3.2.1. Initial (hot-rolled and coiled) conditions

The elemental distribution in the initial microstructures was studied using WDX on areas as large as 120 × 120 µm. In case of the P + F microstructure, the carbon is distributed in big pearlite islands and in small carbides (cf. Fig. 4(a)). The B + M microstructure (cf. Fig. 4(c)) shows a much more homogeneous distribution of the carbon-rich phases. The WDX mapping of Mn reveals a big difference between these two materials. In case of the B + M microstructure (cf. Fig. 4(d)) the manganese signal shows band-like inhomogeneities created by solidification segregations. The P + F microstructure shows, beside the solidification segregations, an enrichment of carbides with manganese (Fig. 4(b)). Chromium is distributed in the same way, but on a lower level proportional to its smaller total content. A more detailed inspection of the Mn distribution of the P + F sample shows that not only Mn enriched regions are present in the material, but also depleted zones. The lowest Mn-concentration in these regions is (1.30 ± 0.05) wt.%. Due to the limited spatial distribution of the WDX technique it was not possible to resolve the elemental distribution inside the pearlite islands.

Fig. 5 presents the results obtained from an extraction replica of the P + F microstructure. Fig. 5(a) shows an STEM image (obtained in an SEM) of the microstructure. Carbide lamellae from the former pearlite and the globular shaped carbides lying in the ferrite matrix are visible. Some of the lamellae are lying on top of each other and, therefore, do not give results for the subsequent EBSD and EDX

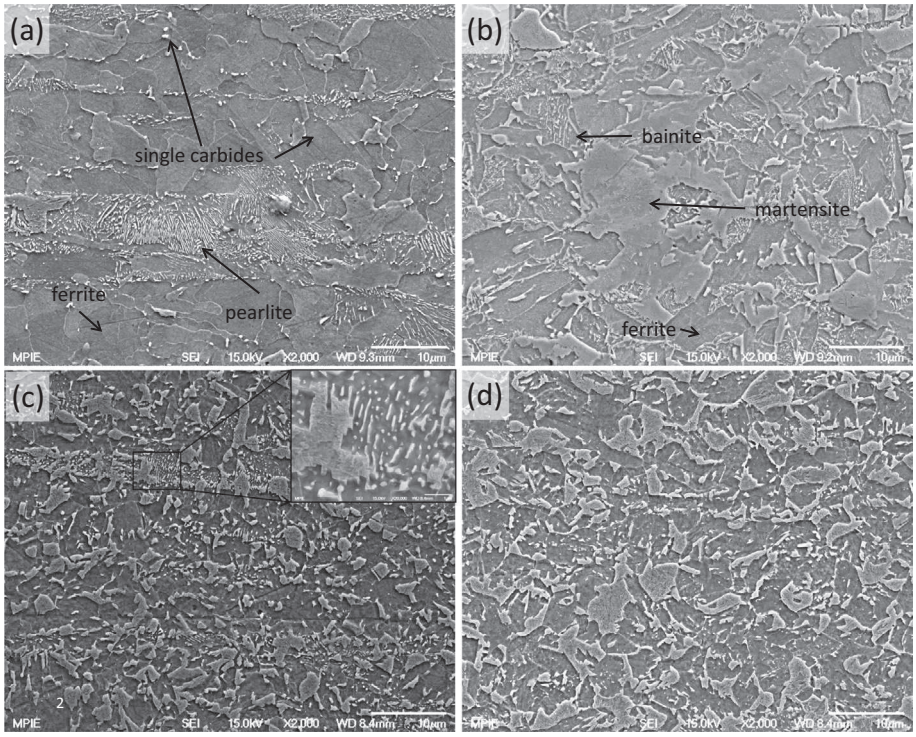

Fig. 2. SEM images of the microstructure at different points of the heat treatment. (a) P + F variant and (b) B + M variant in hot-rolled and coiled condition. (c) P + F variant and (d) B + M after complete heat treatment.

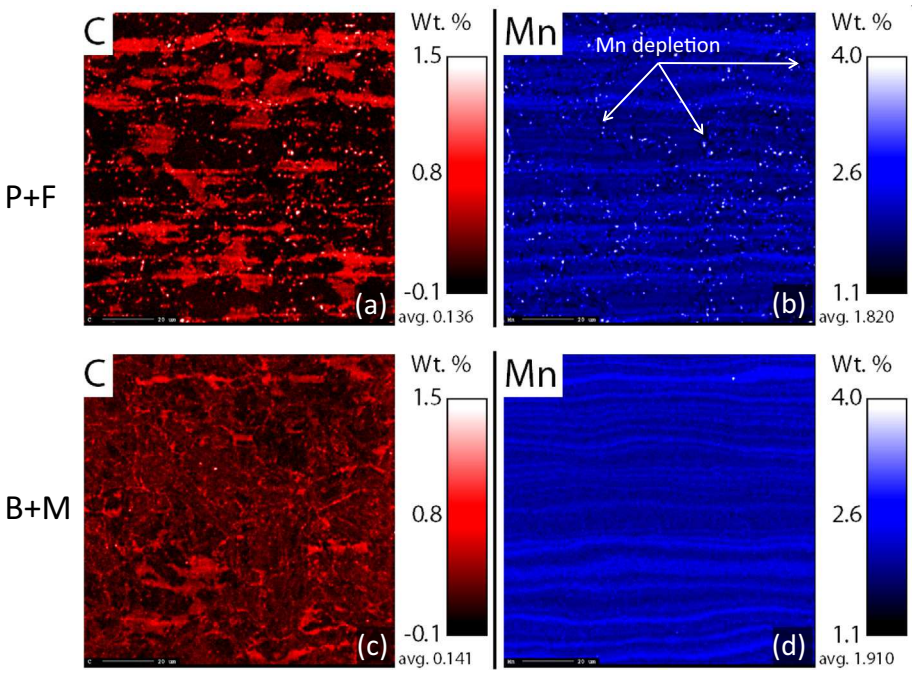

Fig. 4. WDX measurement of P + F (a and b) and B + M (c and d) in hot-rolled and coiled conditions (Point 1 in Fig. 1). Measurement conditions: 300 nm step size, 40 nA beam current, 12 kV, 1 detector for C and 2 detectors for Mn.

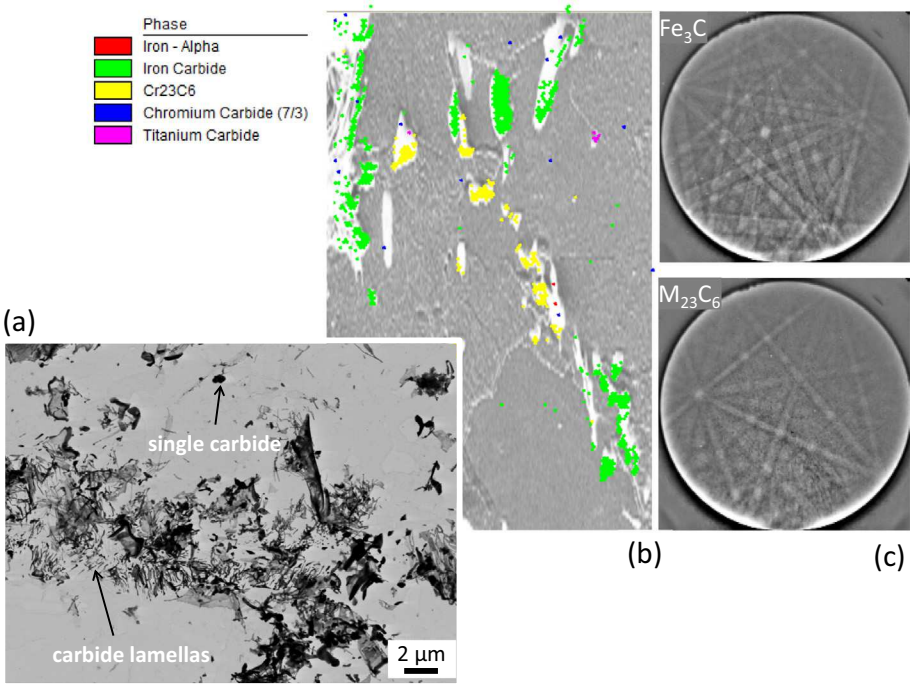

Fig. 5. Results of EBSD measurements performed on the extraction replica created from P + F. (a) Transmission scanning electron micrograph, (b) phase map, obtained by EBSD orientation mapping, (c) examples of patterns: top: cementite, bottom: $M_{23}C_6$.

analysis. EBSD measurements presented in Fig. 5(b) reveal that not only the expected cementite is present in the material, but also $M_{23}C_6$; both can be distinguished by their different crystal structures (cf. Fig. 5(c)). Cementite has an orthorhombic crystal structure [46], while $M_{23}C_6$ has an fcc structure [47]. To determine the exact composition of both carbides, EBSD and EDX were used in combination. Results of these measurements are compiled in Table 1. Both types of carbides are strongly enriched with Mn und Cr but for $M_{23}C_6$ the enrichment is slightly higher than for cementite. In the case of the P + F microstructure also the cementite present in the pearlite is enriched with substitutional elements. In the extraction replica of the B + F microstructure all present carbides are cementite. Their concentration of substitutional elements is close to the composition of the matrix, thus no

Table 1
Composition of the different iron carbides in B + M (bainite + martensite) and P + F (pearlite + ferrite). Values were derived by EDX. The error values are the standard deviation. The carbon content of the carbides has not been measured but stoichiometric composition has been assumed.

	Fe (wt.%)	Mn (wt.%)	Cr (wt.%)
P + F Fe_3C	77.4 (±1)	13.4 (±1)	2.4 (± 0.3)
P + F $M_{23}C_6$	73.0 (±1)	18.1 (± 0.7)	3.5 (± 0.3)
B + M Fe_3C	90.9 (±0.3)	1.9 (± 0.2)	0.4 (± 0.1)

segregation is measured. For both materials the extraction replicas show a huge amount of titanium-carbonitrides.

3.2.2. Isothermally annealed and quenched condition

At point 2 of the heat treatment the manganese distribution in the B + F microstructure did not change (cf. Fig. 6(a) and (b)), but the carbon in the material is now equalized. Only titanium-carbo-nitrides are still present, indicated by a correlation of the carbon and the titanium WDS signal. The otherwise homogenous distribution of carbon indicates a full austenitization of the steel. In case of the P + F microstructure (Fig. 6(c) and (d)) the manganese-enriched and depleted zones are still present, while carbon is distributed much more homogenously. There are, however, a few regions (3% of the measured area), which have a lower content of carbon then the average. A comparison of the manganese and the carbon signal reveals that the manganese depleted zones always correspond to the carbon depleted regions. It is therefore assumed (and proved later by simulations) that the areas of lower carbon content correspond to non-dissolved ferrite caused by their low Mn-content.

3.2.3. Fully heat treated condition

After complete heat treatment (point 3, Fig. 1) both microstructures show a typical DP-microstructure consisting of a ferrite matrix and martensite islands (cf. Figs. 2 and 7). In the case of the P + F microstructure, the WDS-maps show that the manganese and the carbon distribution are correlated (cf. Fig. 7(a) and (b)). Zones enriched or depleted of manganese always correspond to zones enriched or depleted of carbon. In case of the B + M structure the arrangement of carbon is different (cf. Fig. 7(c) and (d)). The carbon rich zones are bigger compared to P + F and borders of the martensite islands exhibit a higher level of carbon than their central regions. XRD-based measurements of the retained austenite, reveal a slightly higher austenite volume fraction for the P + F microstructure than for B + M (B + M: 2 ± 0.4%; P + F 2.9 ± 0.4%), even though both austenite contents are very small. As shown by EBSD (see also Fig. 9) the retained austenite in the P + F microstructure is often located in zones with high manganese content. However, not at all positions showing a manganese peak, retained austenite was found.

EDX-observations on extraction replica revealed that a small amount ($A_{Fe_3C} = 0.051\%$) of $M_{23}C_6$ or cementite lamellae was still present in P + F material after complete heat treatment. In order to estimate the amount of inherited carbides, the area fraction of carbides revealed after complete heat treatment has to be compared to the area fraction of carbides measured before heat treatment. However, due to overlapping cementite lamellae in extraction replicas of the initial state, it was not possible to determine a reliable area fraction of carbides by applying large area EDX mappings. Therefore, the cementite area fraction of the initial material was estimated assuming that all carbon is bound in cementite and that ferrite and cementite have the same density. The area fraction of cementite, A_{Fe_3C}, can then be described by

$$A_{Fe_3C} = \frac{c_{C\text{-}steel}}{c_{C\text{-}Fe_3C}}.$$

$c_{C\text{-}steel}$ is the average concentration of carbon in the steel in wt.% and $c_{C\text{-}Fe_3C}$ is the concentration of carbon in cementite in wt.% (6.67 wt.%). With $c_{C\text{-}steel} = 0.138$ wt.% a value of $A_{Fe_3C} = 2.1\%$ is obtained. This means that only 2.4% of the original amount of carbides was inherited in the P + F material.

3.3. Results of the EBSD measurements

For both microstructures large area EBSD scans were performed. The grain size of ferrite, the kernel average misorientation (KAM) and the martensite content were determined. In the case of

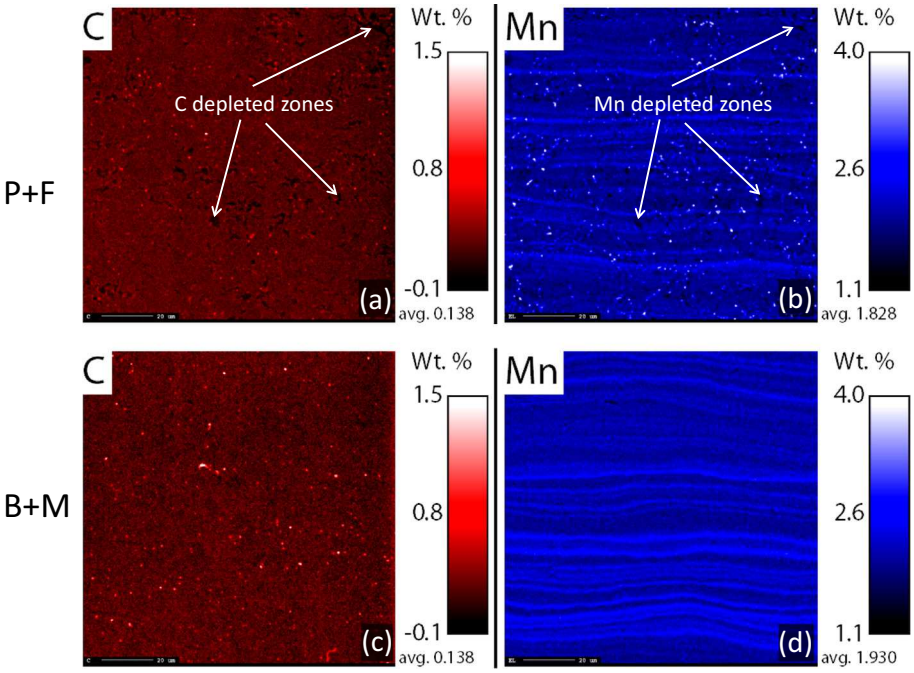

Fig. 6. WDX measurement of P + F (a and b) and B + M (c and d) in isothermally annealed and quenched conditions (Point 2 in Fig. 2). Measurement conditions as in Fig. 4.

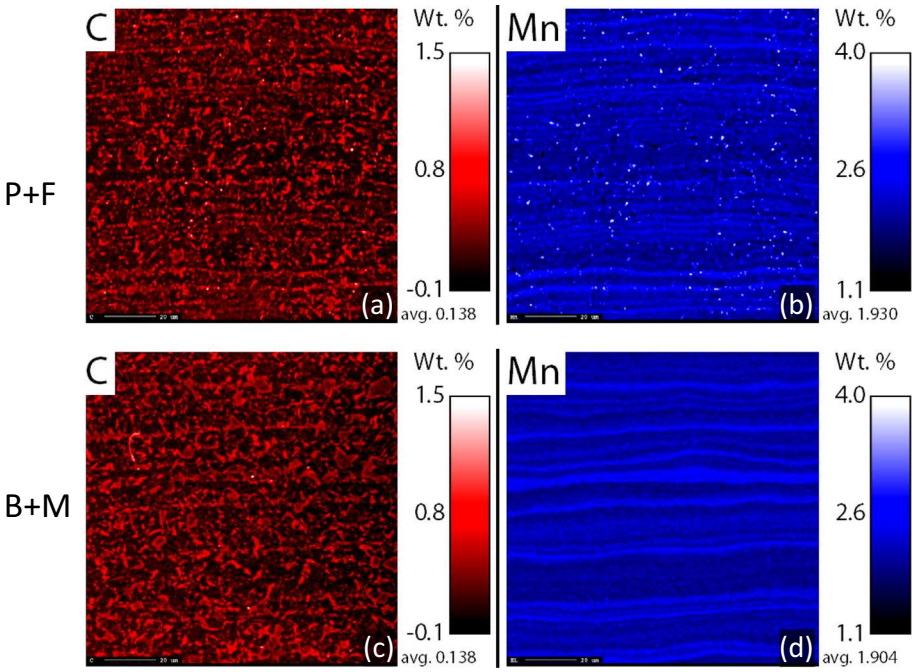

Fig. 7. WDX measurement of P + F (a and b) and B + M (c and d) in fully heat-treated conditions (Point 3 in Fig. 2). Measurement conditions as in Fig. 4.

Table 2
Results obtained from EBSD maps.

	Ferrite grain avg. diameter (μm)	Martensite area fraction (%)	α-iron average GND density $\left(\frac{1}{m^2}\right)$	Ferrite average GND density $\left(\frac{1}{m^2}\right)$
P + F	4.92	7.3 ± 1	$2.53 \cdot 10^{14} \pm 0.5 \cdot 10^{14}$	$2.34 \cdot 10^{14} \pm 0.4 \cdot 10^{14}$
B + M	4.30	14.6 + 1.2	$3.44 \cdot 10^{14} \pm 0.14 \cdot 10^{14}$	$3.09 \cdot 10^{14} \pm 0.14 \cdot 10^{14}$

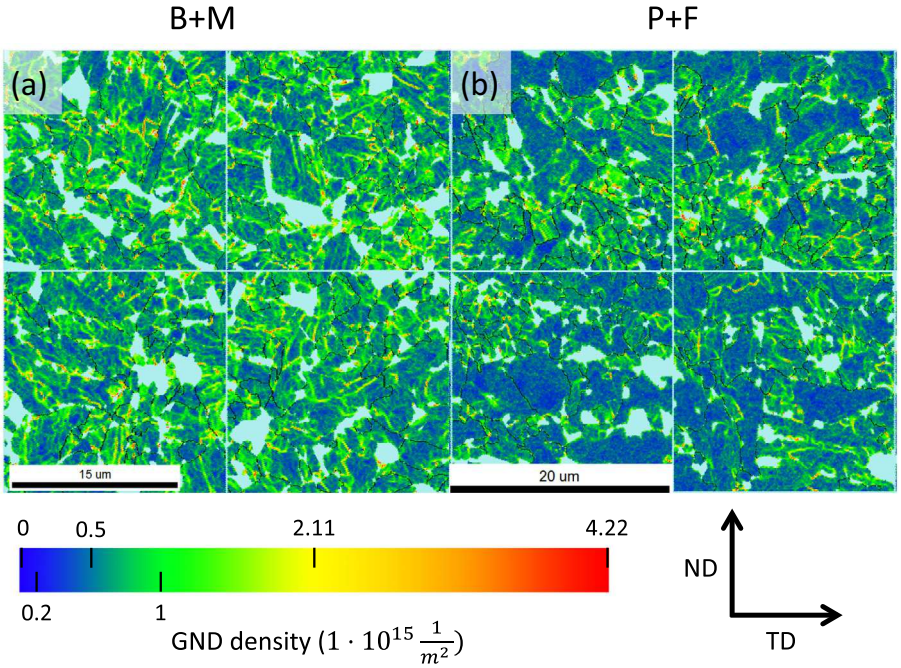

Fig. 8. Example of the GND (geometrically necessary dislocation) density distribution in (a) B + M and (b) P + F. The light blue lines indicate the boundaries between individual maps of the large area scan, the light blue regions in the maps highlight martensite. Large angle boundaries are indicated by black lines.

the P + F microstructure 95 maps with an edge length of about 20 μm were obtained. They were distributed on a rectangle of 1100 × 670 μm. In total, 6385 ferrite grains were analysed to determine the KAM and the average grain size. For B + M, the size of the individual maps was the same. Here, 34 maps were measured. They were distributed over a rectangle of 7750 × 330 μm.

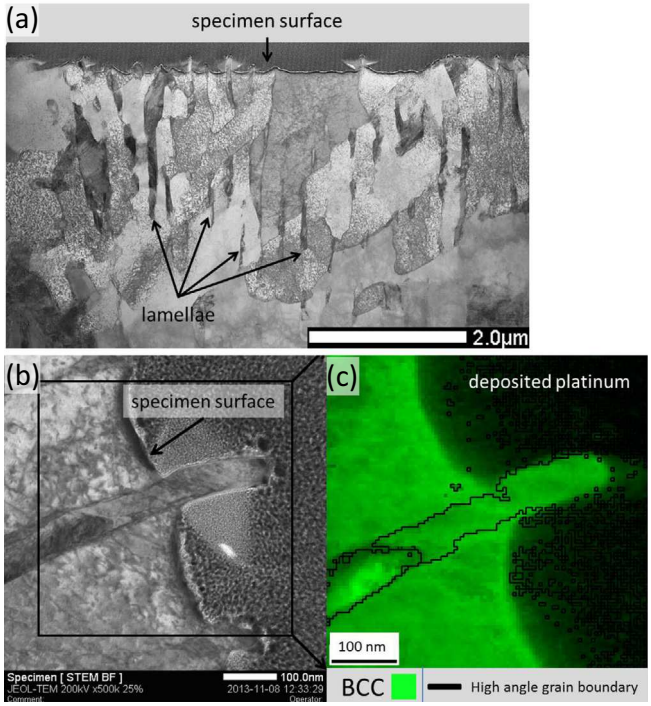

Fig. 9. TEM cross-sectional analysis of the lamellae present in P + F after complete heat treatment. (a) High resolution STEM-image of the lamellae. (b) STEM-image of a single lamella. (c) Result of TEM orientation mapping performed with an ASTAR-system (automated spot-pattern analysis).

The α-iron was separated into ferrite and martensite. 2284 ferrite grains were analysed and KAM values and average grain size were extracted. In order to derive the GND density, Eq. (1) was used. Results of the measurements are presented in Table 2. It shows that the B + M microstructure has a higher content of martensite compared to P + F. The average GND density shows higher values as well, not only in the case of the total α-phase (including martensite) but also for the ferrite constituent alone. The grain size of ferrite found for B + M is slightly smaller than that found for P + F.

Fig. 8 displays two small GND density maps, taken out of the large scans, characteristic of P + F and B + M samples. Here, only the GND density of the ferrite grains is plotted. It is obvious that the GND density is not distributed in the same way in both microstructures. The P + F material contains grains with high GND density and grains with low values. For the B + M material the GND density is high in all ferrite grains.

3.4. Lamellae in P + F after complete heat treatment

In Section 4.2 it was shown that the P + F sample contains only a small amount of inherited carbides. This is somehow in contradiction with the observations of a high amount of lamella structures in this sample, as shown in Fig. 2(c). In order to determine the nature of these lamellae, a TEM-sample was created by FIB target preparation from an etched sample. To this end a platinum layer was deposited on the rough surface of a lamella area. Subsequently a sample was cut out from this area and thinned by FIB. Fig. 9(a) shows an overview of the microstructure in diffraction contrast. The lamellae appear darker than the matrix. On the former specimen surface, some of the deposited platinum covers the lamellae sticking out of the surface. Orientation imaging microscopy was performed on the lamellae using an ASTAR-system [40,41]. Figs. 9(b) and (c) show a single lamella analysed with ASTAR. All lamellae turned out to show only the bcc crystal structure; neither austenite, cementite nor other Fe carbides were found.

3.5. Analysis of the dilatometer curves

Fig. 10 displays two temperature-elongation curves measured by dilatometry on the two different microstructures. Altogether 5 measurements were performed for each material. During heating up, the growth of austenite is indicated by a sudden change of the slope of the curve. The average start temperature for B + M is (737 ± 4) °C and (755 ± 3) °C for P + F. This indicates that for both microstructures the growth of austenite starts at nearly the same temperature. In contrast, the cooling curves show distinct differences between both materials. In the case of the P + F microstructure the transformation of fcc to bcc begins much earlier than in the case of B + M. The exact transformation temperature for B + M is 510 ± 1 °C and 668 ± 8 °C for P + F. Here, the error is the standard deviation of 5 measurements. The martensite start temperature was determined for both variants as well. For B + M it is 225 ± 23 °C and for P + F 161 ± 12 °C.

4. Discussion

To make an appropriate discussion it is reasonable to summarize the results as follows:

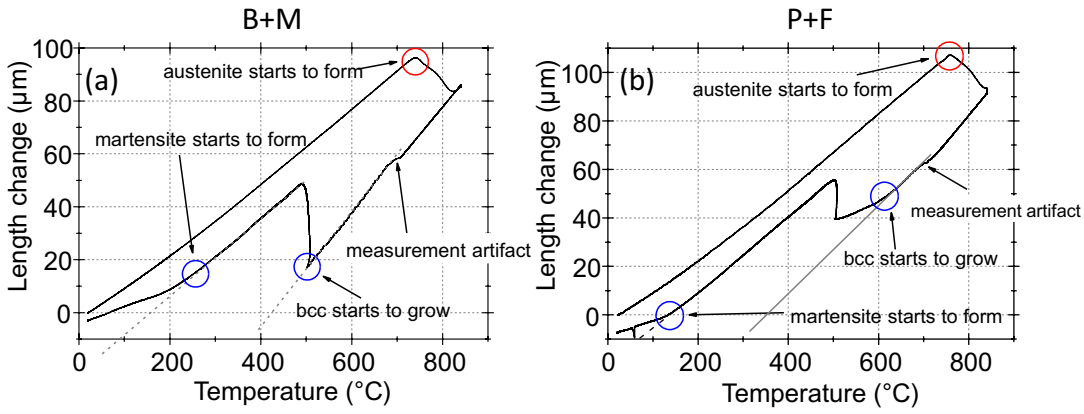

Fig. 10. Dilatometer curves obtained during heat treatment of (a) B + M, (b) P + F. The red circle indicates the transformation to austenite. The blue circles show at which temperature bcc and martensite start to grow. The measurement artefact is caused by the change of cooling speed occurring at this temperature. (For interpretation of the references to color in this figure legend, the reader is referred to the web version of this article.)

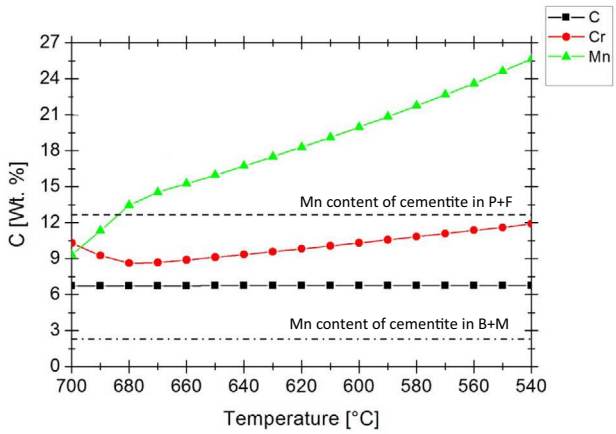

Fig. 11. Equilibrium concentration of M_3C depending on temperature. The average composition of P + F was used to calculate the concentrations with TC (Thermo-Calc). Other carbides than cementite were not taken into account and therefore not allowed to occur. The dashed and dashed-dotted lines indicate Mn-levels of the cementite in the initial P + F and B + M material as measured by EDX (e.g. after coiling).

- The main difference between the two initial microstructures obtained after coiling at different temperatures is the distribution of manganese. For B + M, coiled at lower temperature, manganese only shows heterogeneities in the form of solidification segregations. For P + F, coiled at higher temperatures, manganese is enriched in carbides and depleted in other zones. The local heterogeneities survive the heat treatment, even though the carbides responsible for them are nearly completely dissolved.
- Before heat treatment, the B + M microstructure is harder than P + F. Interrupting the heat treatment after the isothermal annealing step leads to microstructures that have both the same hardness. After complete heat treatment, B + M is again harder than P + F.
- For P + F the reaustenization is not completed after holding the material at the temperature plateau. This is indicated by carbon and Mn-depleted zones, which correspond to untransformed ferrite.
- During cooling down, the fcc–bcc transformation begins at about 160 K higher temperatures for P + F than for B + M. After complete heat treatment the martensite content for B + M as well as the average GND density in α-iron and ferrite is higher.
- After complete heat treatment the P + F microstructure shows lamella-like areas, which appears like incompletely dissolved pearlite. Extraction replica and EBSD measurements show, that these lamellae are neither cementite nor $M_{23}C_6$ but austenite or martensite. Only 2.6% of the original amount of carbides is inherited.

4.1. Enrichment of carbides with substitutional elements during coiling

The initial material shows carbides that have been enriched to different levels of substitutional elements after coiling at different temperatures. The enrichment is, in most cases, related to a similar substitutional element depletion of the matrix surrounding the carbides. This heterogeneous distribution of Mn must have been created during coiling of the material as neither chemical composition nor any other production parameter is different between the two materials.

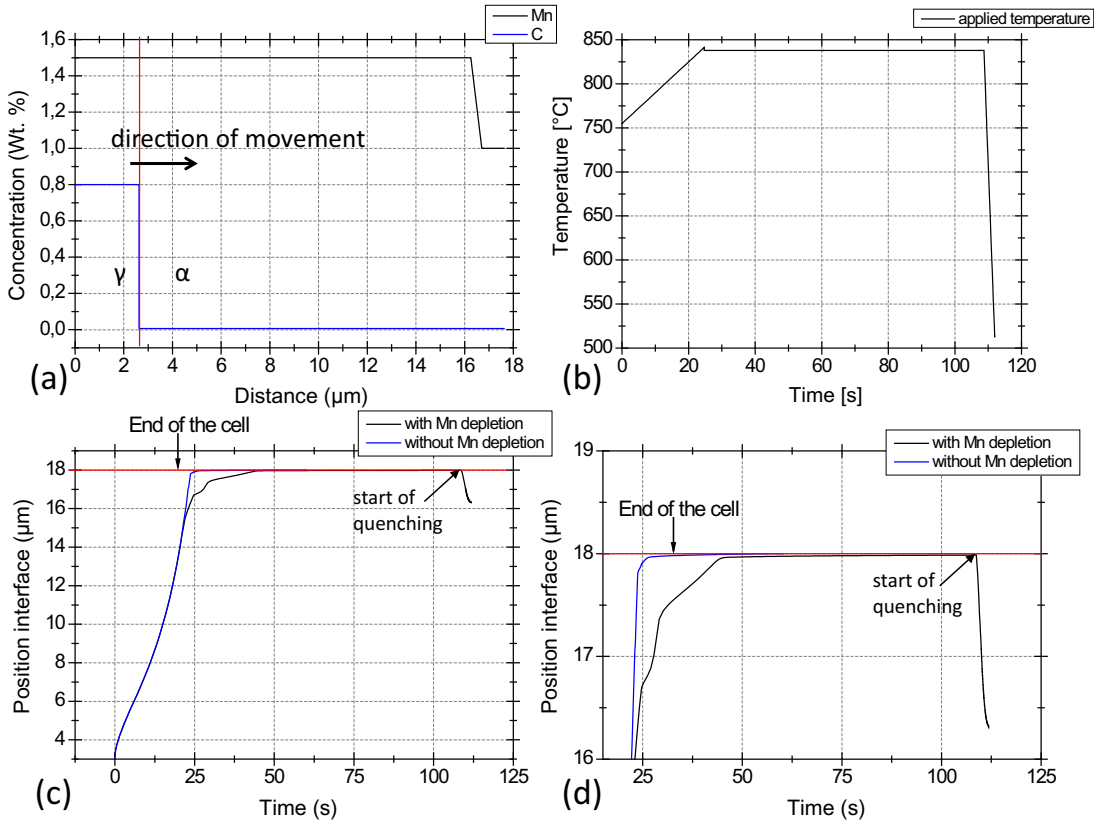

Fig. 12. Results of the DICTRA simulation performed to study the influence of the Mn depleted regions. (a) Start distribution of the alloying elements. (b) Evolution of the temperature with time. (c) Position of the gamma–alpha interface in dependence of time. (d) Magnified version of (c). The red line indicates the end of the cell. A planar geometry was used for the simulation.

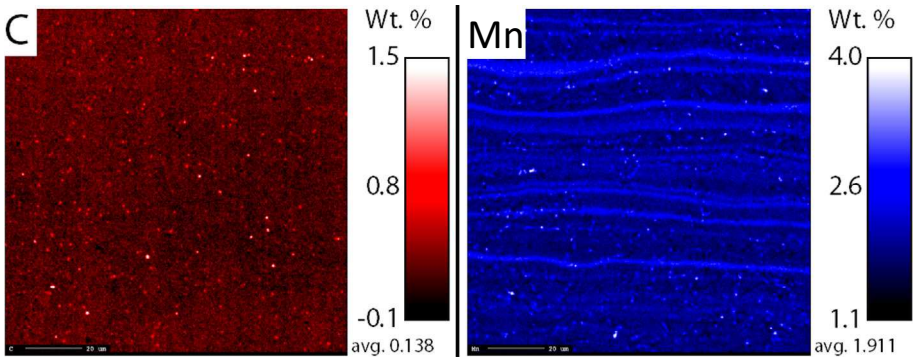

Fig. 13. WDX measurement of P + F annealed at 1173 K and quenched (Point 2). (a) Distribution of carbon. (b) Distribution of Mn. Measurement conditions as in Fig. 4.

It is established knowledge that carbides can be enriched with substitutional elements like Mn and Cr [27–29]. Fig. 11 shows the equilibrium enrichment of cementite with substitutional elements in dependence of the temperature for the present material, as calculated with TC. It is noted that the lower the temperature the higher the enrichment of M_3C with substitutional elements in equilibrium. It should be noted, however, that the high value of Mn-concentration obtained for low temperatures in the calculation, is due to the fact that the simulations were done excluding the formation of other carbides than cementite. Of course, due to limited diffusion, these values are not found in real samples. The dashed line shows the degree of Mn enrichment in the analysed cementite in P + F and the dashed-dotted line shows the enrichment measured in B + M. For B + M the concentrations of the substitutional elements is close to the average concentration of the steel. For this case it can be concluded that the temperature during which the carbides were formed was too low to allow the formation of carbides following local equilibrium with partitioning (LEP). The formation must have occurred under local equilibrium with no partitioning (LENP) or paraequilibrium (PE). In contrast, the higher temperature of coiling for P + F allowed a transformation according to LEP, resulting in higher Mn content of the carbides and depletion of the surrounding matrix.

4.2. Evolution of hardness during heat treatment

After complete heat treatment the B + M microstructure has a higher hardness than the P + F microstructure. This observation can be rationalized by two facts. First, B + M contains more martensite and it is well known that martensite hardens the material [3]. Second, B + M also shows a higher GND density as compared to P + F. GNDs represent forest dislocations for mobile dislocations and, therefore, harden the material (e.g. Ashby et al. [48]). The question arises, which mechanism causes the higher GND content in the B + M material.

As already mentioned, the plateau temperature of the applied heat treatment was at 1113 K. The phase diagram of the steel reveals that austenite is the only stable phase at this temperature. WDX measurements performed after quenching the material (point 2 of the heat treatment) revealed, however, that in the case of the P + F microstructure reaustenization was not completed, indicated by the fact that some regions have a significantly lower carbon content than the average (cf. Fig. 6). During cooling down of P + F, ferrite started to grow at significantly higher temperatures (668 °C ± 8 °C) compared to B + M (510 °C ± 1 °C). The reasons for this are the areas of inherited, untransformed ferrite, which can start to grow during cooling down without any nucleation. Similar observations have been reported, e.g. in [49] on ferrite/bainite in TRIP steels. In the case of B + M, no ferrite survived the isothermal part of the heat treatment. Hence, new ferrite had to nucleate during cooling down. In general, nucleation processes need time and a certain degree of undercooling, which means that in the case of B + M the transformation of fcc to bcc begins at a lower temperature compared to P + F.

It is very likely that the dissimilar martensite content of both variants is a result of the different growth temperatures of bcc for P + F and B + M. Compared to P + F, the ferrite in B + M has less time to grow and the diffusional growth of ferrite is limited due to

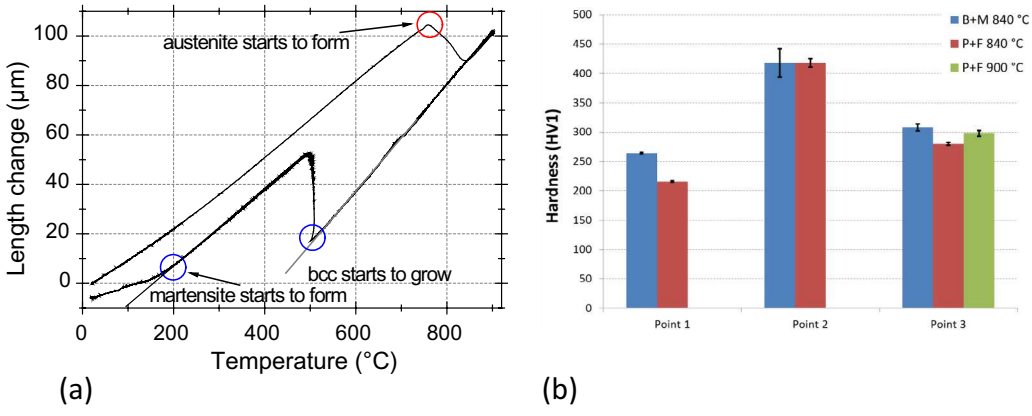

Fig. 14. Results of the alternative heat treatment experiments performed on P + F. (a) Dilatometer curve elongation vs. temperature. (b) Hardness of the material at different points of the heat treatment (green bar) as compared to the initial heat treatments (same data as Fig. 4) (red and blue bars). (For interpretation of the references to colour in this figure legend, the reader is referred to the web version of this article.)

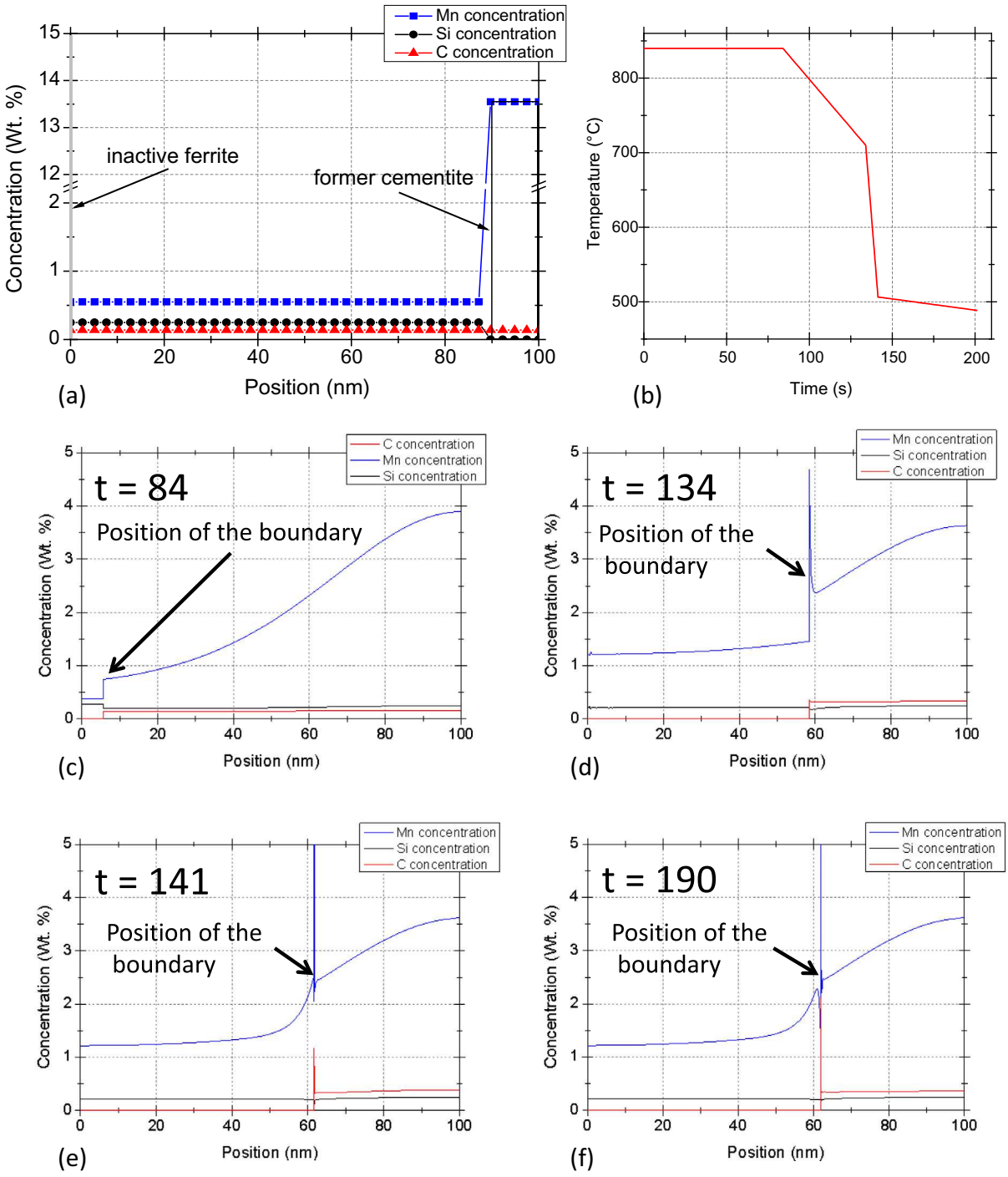

Fig. 15. DICTRA simulations of the temporal and lateral evolution of the lamella structure found in P + F after complete heat treatment. (a) Initial distribution of the elements; the complete cell is austenitic. (b) Applied heat treatment. (c–f) Evolution of the distribution of the substitutional elements with time. The arrow indicates the position of the α–γ-boundary. Regions with low carbon content, left of the boundary, are ferrite.

the lower mobility of all elements at the lower temperature. This leads to a higher content of austenite, which transforms to martensite during cooling down to room temperature.

The different growth temperatures of bcc for P + F and B + M also appear to be the reason for the lower values of the average GND density in ferrite in P + F. Indeed, the lower the temperature of the γ–α transformation the more it changes from a diffusional to a displacive character. A displacive transformation, in turn, produces shape accommodation dislocations as it is well known for the formation of martensite. For a bainitic transformation, which is partly diffusive and partly displacive it was shown, furthermore, that the bcc phase formed at higher temperatures has a lower dislocation than the one formed at lower temperatures [50]. We, therefore, claim that the observed difference in dislocation densities between the B + M and P + F samples is caused by a change in the transformation character from diffusive to displacive. This hypothesis has recently been investigated in more detail by the authors (to be published).

In comparison to the other effects, the inherited carbides influence the hardness of P + F only marginally. For P + F it was shown

that only 2.4% of the original amount of carbides was inherited. This implies that most of the carbon is available for martensite hardening.

4.3. Simulation of the role of Mn depleted zones on the fcc to bcc transformation

In order to understand the origin of the non-dissolved ferrite in the P + F microstructure, one has to take a closer look at the elemental distribution obtained at point 2 of the heat treatment. As shown in Fig. 6, low carbon regions correlate in most cases with low Mn regions. A lower concentration of Mn increases the γ–α transformation temperature and, therefore, reduces the α–γ transformation rate. In order to prove whether a manganese-depleted zone with a Mn content of 1 wt.% could slow down the interface between austenite and ferrite long enough to allow the ferrite to prevail during the isothermal part of the heat treatment, the following DICTRA simulation was set up: The size of the simulation cell was set to 18 μm, which is half of the longest distance measured by SEM between two pearlite regions. The start temperature was set to 755 °C at $t = 0$ s corresponding to the temperature at which the dilatometer curves showed the start of the reaustenization for the P + F microstructure. It was assumed that at this temperature all pearlite that was present in the material had already transformed into austenite with a carbon concentration corresponding to that of the average pearlite concentration. Such a transformed area served as austenite nucleus in the cell. The initial distribution of C and Mn, and of the phases is plotted in Fig. 12a: The Mn content is the same (1.5 wt.%) everywhere except for the right part of the ferrite region which serves to simulate a Mn-depleted zone. The average carbon content of the cell was set to 0.138 wt.% except for the area of the austenite nucleus. This cell was then subjected to heat treatment, shown in Fig. 12b, consisting of ramping up to 834 °C in 25 s, holding at that temperature for 90 s and finally quenching at a rate 100 K/s. A second simulation for a cell without Mn-depletion was also set up using the same conditions as those of the first one. Results of both simulations are shown in Fig. 12(c) and (d). For the simulation of the cell with Mn depletion, the interface reached the depleted zone after 60 s. There the transformation rate became very low and, as a result, a small part of the ferrite region was conserved to the end of the isothermal annealing. During quenching, this ferrite region started to grow again and reached a total thickness of 1.7 μm. Because only half of a Mn depleted zone was simulated, the total thickness of the ferrite region is 3.4 μm. For the simulation without Mn depletion the results differed significantly. As it can be seen in Fig. 12(c) or (d), the interface was also fast in the beginning and slower after a few seconds, but ferrite was not stabilized. After 60 s, which means after roughly 35 s of the isothermal part, the ferrite was completely dissolved. As a consequence, no ferrite could grow during quenching.

4.4. Alternative heat treatment of P+F for full austenization

In order to investigate whether the incomplete austenization is indeed the reason for the change of properties after cooling, an alternative heat treatment was applied with higher austenization temperature of 900 °C. The WDS measurement after interrupting the heat treatment (Fig. 13) now shows a homogeneous distribution of carbon even in the Mn depleted zones. This indicates complete austenization of the material. The dilatometer curve of this specimen (Fig. 14(a)) now reveals a lower γ–α transformation temperature, comparable to that of the B + M microstructure. Also the hardness of the material increases (Fig. 14(b)) and is much more comparable to the hardness of the B + M microstructure after complete heat treatment.

4.5. The nature and origin of the lamellae found in P + F after complete heat treatment

After complete heat treatment lamellae were found (Fig. 2(c)) which appeared like partly dissolved pearlite. However, the investigation of the extraction replicas showed that nearly no carbon rich carbides like cementite survive the heat treatment. Rather, retained austenite and martensite are found at the positions of the lamellae. In order to understand the origin and formation of these special microstructures, DICTRA calculations were performed. These calculations also help understanding why no new carbides form during cooling.

The analysis of the extraction replica of the initial state of the P + F microstructure shows an enrichment of the carbides, even in pearlite, with manganese. Even though the carbides dissolve during the heat treatment, WDS measurements show that the Mn-enrichments survive the complete heat treatment. To analyse the diffusion of a Mn enrichment caused by pearlite with time, a DICTRA simulation was set up as follows: The simulation starts at the beginning of the plateau of the heat treatment. The complete time–temperature curve can be seen in Fig. 15(b). It is assumed that the pearlite microstructure is fully austenitic, but the Mn-enrichments caused by the carbides are still present. Our experiments showed that these initial conditions are reasonable:

During heating up to 840 °C the dilatometer curves of P + F indicate a nearly complete austenization of the matrix.

SEM image of P + F, taken after interrupting the heat treatment during heating up at 765 °C, showed, that pearlite is the first to transform to austenite at the beginning of the phase transformation. This growth mechanism is also reported by several other studies.

The starting conditions of the simulations are displayed in Fig. 15(a). The degree of Mn-enrichment, used for the simulation, is set to the same value as the one measured with EDX in pearlite. The enrichment is located at the right end of the simulated cell. It has the same thickness as a typical cementite lamella. It is important to note that the former carbide is virtually free of silicon caused by the very low solubility of Si in the carbide [51]. Non-enriched austenite is located at the left side of the former cementite. It has half the thickness of the typical distance of two cementite lamellae in perlite. An inactive bcc phase is located at the left side of the cell which serves as a nucleus for phase transformation. It starts to grow as soon as it becomes thermodynamically stable. LEP/LENP was used as growth regime, which means that partitioning of the substitutional elements is taken into account. Fig. 15(c–f) displays the distribution of the elements at different times. At the end of the isothermal part of the simulation after $t = 84$ s, carbon is still found at the position of the former cementite lamella, but at a low level. The Mn enrichment strongly redistributed, but the enrichment is still significant. Special attention has to be paid to the distribution of the silicon. At the beginning there is no silicon at the position of the former cementite; however, after the isothermal holding it is even enriched at zones of former cementite. This means that once the pearlite is dissolved, it is very unlikely that new pearlite forms due to the low mobility of silicon at lower temperatures and the fact that cementite has practically no solubility for silicon. During cooling down, the bcc phase starts to grow fast and reaches its maximum extension at $t = 134$ s. At that moment a high Mn-concentration peak has been collected at the phase boundary due to the rather slow diffusion of Mn in austenite. After this time, no more growth of bcc iron is observed because the Mn diffusion into the austenite becomes too slow to allow the progression of ferrite. As a consequence austenite is kinetically stabilized. During quenching down to room temperature, this austenite may then either transform to martensite or be retained as metastable austenite.

5. Conclusions

The present study shows the importance of the initial distribution and diffusion of substitutional elements for the formation of DP microstructures during their heat treatment process. The main results and conclusions are summarized below.

The coiling temperature may drastically influence the enrichment of carbides with substitutional elements like manganese and chromium. High temperatures lead to a high degree of enrichment (P + F). Material coiled at lower temperatures does not contain any enriched carbides (B + M). The most likely reason for this behaviour is the change of the growth regime of carbides from LEP to LENP or PE.

In case of P + F, it was found that Mn enriched regions occur correlated with Mn depleted zones. These zones retard the α–γ transformation and lead to an incomplete austenization during the applied heat treatment. It was shown with DICTRA that Mn depleted zones have a retarding effect on the growth of austenite during austenization. It was revealed that the ferrite regions are only kinetically stabilized. A longer or higher temperature heat treatment leads to complete austenization.

During cooling down, the B + M material transforms at lower temperatures from austenite to ferrite than the P + F material. The reason for this is that nucleation of new ferrite is needed in the case of B + M. In contrast, for P + F no nucleation of ferrite is needed, due to the incomplete austenization. The retarded transformation of B + M leads to a higher density of geometrically necessary dislocations as well as to a higher martensite content. Both contribute to the higher hardness of B + M compared to P + F.

During isothermal holding the carbides dissolve, but the related Mn-enrichments do not homogenize completely. After the complete heat treatment there is a higher chance to find retained austenite at regions of higher Mn content. This does not only apply to former globular carbides but also to pearlite islands. The microstructure thus resembles the original pearlite but the former cementite lamellae now consist of austenite or martensite. DICTRA calculations show the austenite-stabilizing effect of Mn-enrichments during cooling. They show furthermore that Si homogenizes fast enough to prevent the formation of fresh cementite.

Acknowledgement

The authors would like to express their gratitude to ThyssenKrupp Steel Europe for the financial support of the work and the fruitful discussions.

References

[1] M.S. Rashid, Annu. Rev. Mater. Sci. 11 (1981) 245.
[2] J. Zrnik, I. Mamuzic, S.V. Dobatkin, Metalurgija 45 (2006) 323.
[3] R.G. Davies, F.M. Company, Metall. Trans. A 9 (1978) 671.
[4] N.K. Balliger, T. Gladman, Met. Sci. 15 (1981) 95.
[5] M. Sarwar, R. Priestner, J. Mater. Sci. 31 (1996) 2091.
[6] G.R. Speich, V.A. Demarest, R.L. Miller, Metall. Trans. A 12A (1981) 1981.
[7] X. Cai, J. Feng, W.S. Owen, Metall. Trans. A 16A (1985) 1405.
[8] F.M. Al-Abbasi, J.A. Nemes, Int. J. Mech. Sci. 45 (2003) 1449.
[9] P. Deb, M.C. Chaturvedi, Mater. Sci. Eng. 78 (1986) L7.
[10] M. Calcagnotto, D. Ponge, D. Raabe, ISIJ Int. 52 (2012) 874.
[11] O. León-García, R.H. Petrov, L.A.I. Kestens, Mater. Sci. Forum 638–642 (2010) 3337.
[12] M. Calcagnotto, D. Ponge, Y. Adachi, D. Raabe, Proc 2nd Int Symp Steel Sci (ISSS 2009), 2009, p. 1.
[13] M. Calcagnotto, D. Ponge, D. Raabe, Mater. Sci. Eng., A A 527 (2010) 7832.
[14] A.G. Preban, Chicago E 33 (1985) 897.
[15] M. Delincé, Y. Bréchet, J.D. Embury, M.G.D. Geers, P.J. Jacques, T. Pardoen, Acta Mater. 55 (2007) 2337.
[16] X.P. Shen, R. Priestner, Metall. Mater. Trans. A 21A (1989) 2547.
[17] C.C. Tasan, J.P.M. Hoefnagels, M. Diehl, D. Yan, F. Roters, D. Raabe, Int. J. Plast. 63 (2014) 198.
[18] C.C. Tasan, M. Diehl, D. Yan, C. Zambaldi, P. Shanthraj, F. Roters, et al., Acta Mater. 81 (2014) 386.
[19] M. Kulakov, W.J. Poole, M. Militzer, Metall. Mater. Trans. A 44 (2013) 3564.
[20] N.C. Goel, J.P. Chakravarty, K. Tangri, Metall. Trans. A 18 (1987) 5.
[21] F.G. Caballero, C. Capdevila, C.G.D.E. Andrés, ISIJ Int. 41 (2001) 1093.
[22] X. Cai, W.S. Owen, Metall. Trans. A 16 (1985) 543.
[23] F.G. Caballero, A. García-Junceda, C. Capdevila, C. García de Andrés, Mater. Trans. 47 (2006) 2269.
[24] C.C. Tasan, J.P.M. Hoefnagels, M.G.D. Geers, Scripta Mater. 62 (2010) 835.
[25] J.D. Verhoeven, J. Mater. Eng. Perform. 9 (2000) 286.
[26] T.F. Majka, D.K. Matlock, G. Krauss, Metall. Mater. Trans. A 33 (2002) 1627.
[27] S.A. Al-Salman, G.W. Lorimer, N. Ridley, Metall. Trans. A 10A (1979) 1703.
[28] G. Miyamoto, H. Usuki, Z.-D. Li, T. Furuhara, Acta Mater. 58 (2010) 4492.
[29] C. Zhu, X.Y. Xiong, A. Cerezo, R. Hardwicke, G. Krauss, G.D.W. Smith, Ultramicroscopy 107 (2007) 808.
[30] M. Calcagnotto, D. Ponge, D. Raabe, Metall. Mater. Trans. A 43 (2011) 37.
[31] A. Borgenstam, L. Höglund, J. Ågren, A. Engström, J. Phase Equilibria 21 (2000) 269.
[32] J. Andersson, T. Helander, L. Höglund, Calphad 26 (2002) 273.
[33] L. Lutterotti, S. Matthies, H.-R. Wenk, Proceeding Twelfth Int Conf Textures Mater – ICOTOM-12, vol. 1, 1999, p. 1599.
[34] D.P. Field, Ultramicroscopy 67 (1997) 1.
[35] P.T. Pinard, A. Schwedt, A. Ramazani, U. Prahl, S. Richter, Microsc. Microanal. 19 (2013) 996.
[36] S.I. Wright, M.M. Nowell, Microsc. Microanal. 12 (2006) 72.
[37] K. Davut, S. Zaefferer, Metall. Mater. Trans. A 41 (2010) 2187.
[38] M. Calcagnotto, D. Ponge, E. Demir, D. Raabe, Mater. Sci. Eng., A 527 (2010) 2738.
[39] L. Kubin, A. Mortensen, Scripta Mater. 48 (2003) 119.
[40] S. Rouvimov, E.F. Rauch, P. Moeck, S. Nicolopoulos, M. Véron, J. Portillo, et al., Microsc. Anal. 22 (2008) S5.
[41] S. Rouvimov, E. Rauch, P. Moeck, S. Nicolopoulos, Microsc. Microanal. 15 (2009) 1290.
[42] F. Eggert, Standardfreie Elektronenstrahl-Mikroanalyse, Books on Demand, Norderstedt, 2005.
[43] E. Eichen, J. Tabock, K.R. Kinsman, Metallography 162 (1972) 151.
[44] D.B. Williams, C.B. Carter, Transmission Electron Microscopy – A Textbook for Materials Science, Springer, 2009.
[45] J.-O. Andersson, T. Helander, L. Höglund, Calphad 26 (2002) 273.
[46] S.K. Tewari, R.C. Sharma, Metall. Trans. A 16 (1985) 597.
[47] C.W. Kuo, C. Fan, S.H. Wu, W. Wu, Mater. Trans. 48 (2007) 2324.
[48] M.F. Ashby, Philos. Mag. 21 (1970) 399.
[49] S. Zaefferer, J. Ohlert, W. Bleck, Acta Mater. 52 (2004) 2765.
[50] H.K.D.H. Bhadeshia, Bainite in Steels – Transformations Microstructure and Properties, second ed., 2001.
[51] E. Kozeschnik, H.K.D.H. Bhadeshia, Mater. Sci. Technol. 24 (2008) 343.